Ultrafast hot carrier injection in Au/GaN: the role of band bending and the interface band structure

Fan Zheng and Lin-wang Wang*

Joint Center for Artificial Photosynthesis and Materials Sciences Division, Lawrence Berkeley National Laboratory, Berkeley, California 94720, USA.

E-mail: lwwang@lbl.gov

Abstract

Plasmon photochemistry can potentially play a significant role in photocatalysis. To realize this potential, it is critical to enhance the plasmon excited hot carrier transfer and collection. However, the lack of atomistic understanding of the carrier transfer across the interface, especially when the carrier is still "hot", makes it challenging to design more efficient system. In this work, we apply the non-adiabatic molecular dynamics simulation to study hot carrier dynamics in the system of Au nanocluster on top of GaN surface. By setting up the initial excited hole in Au, the carrier transfer from Au to GaN is found to be on a sub-pico second time scale. The hot hole first cools to the band edge of Au *d*-states while it transfers to GaN. After the hole has cooled down to the band edge of GaN, we find some of the charges can return back to Au. By applying different external potentials to mimic the Schottky-barrier band bending, the returning charge can be reduced, demonstrating the importance of the internal electric field. Finally, with the understanding of the carrier transfer's pathway, we suggest

that a ZnO layer between GaN and Au can effectively block the "cold" carrier from returning back to Au but still allow the hot carrier to transfer from Au to GaN.

Photochemistry relies on photo generated carriers to execute electrochemical reactions. Recently, plasmon has been used as a potential photo absorber to generate photo carriers.[1–4] Due to the involvement of many electrons in a plasmon excitation, the plasmon mode in a metal nano-system can have much higher optical oscillator strength than a typical semiconductor, thus it has higher light absorbing efficiency. It has also been shown recently that the collective many-particle plasmon excitation can convert its energy into single-particle excitation inside the metal nano-system within 100 fs .[2,5] One way to harvest such single particle hot carrier is to attach the metal nano-system (e.g., a metallic quantum dot, QD) to a semiconductor substrate. In this case, the hot carrier cooling process is accompanied by carrier injection and carrier transfer into semiconductor substrates. Questions arise for the carrier injection process: (1) what determines the competition between the carrier cooling inside the metal-QD and the carrier injection into the substrate? (2) Can the substrate harvest hot carrier instead of equilibrium ones ("cold" carrier) at the band edge, which can be used to drive the hot carrier nonequilibrium reaction? (3) What is the typical time scale for cooling and carrier injection? (4) How the interface electronic structure and band alignment influence the hot carrier injection? Answering these questions are important. For example, a lot of recent effort has been placed to study the possibility of hot carrier catalysis in various redox reactions such as water splitting and oxidation,[6–11] H_2 decomposition or production,[12–14] and CO_2 reduction.[15–17] Thus, designing an efficient way to harvest hot carriers (not just the "cold" carrier) becomes an important research topic.

The reported efficiencies of the plasmon assisted catalytical reactions are generally low.[18–21] Less than 3% solar-to-chemical efficiency is obtained in CsS-Au-TiO_2 sandwich system,[18] which is far below the solar cell light conversion efficiency. In an Au/TiO_2 system, the efficiency of the light induced carrier transferred is only 0.2%.[21] It is possible that only a small portion of hot carriers has been injected into the carrier collection material during their cooling. The transient pump-probe experiments using absorption spectroscopy or non-linear optics techniques show that the time scale of the charge transfer from a quantum dot or

metal cluster to a semiconductor is on the order of sub-pico second.[22–28] However, the exact pictures of such carrier injection and carrier cooling processes are difficult to probe experimentally. To understand such process in the atomic scale, theoretical simulation has been used to study this process .[29–33] For example, Atwater et al estimate the surface plasmon decay rate and the initial hot-carrier distribution in metals using Fermi's golden rule.[29,30] The carrier transport is then evaluated by first-principle method based on electron-electron and electron-phonon scattering. Bernardi and Zhou use perturbation method to compute the electron-phonon coupling.[32,33] Combining with the Boltzmann equation, the carrier mobility and carrier cooling process are revealed in the bulk system. While such methods are excellent in studying bulk systems or interface scattering of large systems, it is not a direct simulation of a nano hetero-system as a whole. Thus, it might be difficult to study the carrier injection in a heterogeneous nano-system. Another analytical approach to study carrier injection is to calculate charge transfer rate with formula like the Marcus theory.[34–38] However, such calculations can only reveal charge transfer for localized carriers and for equilibrium cold carriers instead of hot carriers.

One alternative approach is to simulate the hot carrier cooling and injection directly using nonadiabatic electronic dynamics. In this approach, the time-dependent Schrödinger's equation is followed to directly simulate the change of carrier wavefunction. It is suitable to study nano-systems with about one hundred atoms, thus it is complementary to the analytical studies based on bulk behaviors.[29,30] Pioneer works based on non-adiabatic molecular dynamics or time-dependent density function theory have studied the carrier motion for interfacial systems, such as Dye-sensitized TiO_2,[39,40] Ag (and Au) on MoS_2,[41] Au nanoparticle/nanorod on TiO_2,[42,43] PbSe nanoparticle on TiO_2,[44] bilayer two-dimension heterostructures,[45] and graphene on TiO_2.[46] They all demonstrate the fast carrier transfer within a few hundreds femtosecond across the interface. However, most of these works illustrate the details of the electron transfer from the band edge of a quantum dot, semiconductor or dye to another semiconductor.[39,40,44] Some other works also demonstrate the delocalization across the

metal/semiconductor interface from a plasmon-like adiabatic state near the Fermi level.[42,45] However, in most cases, the transferred carriers are band edge carrier, instead of hot carriers. There are not enough studies of the hot carrier cooling in combination of charge transfer. On the other hand, many works[43,47–49] use nonadiabatic molecular dynamics to study hot carrier cooling (e.g. inside a QD), but no injection process. Thus, there is a lack of study to reveal the competition between hot carrier's cooling and hot carrier injection, and different pathways for hot carrier injections. Furthermore, although Schottky barrier and its related band bending exist in almost all the metal-semiconductor interfaces, a detailed understanding for the role of the Schottky barrier to the carrier transfer is also lacking.

In this work, inspired by the recent experimental work of Au nanocluster on GaN for the plasmon hot carrier injection,[16] we use the non-adiabatic molecular dynamics (NAMD) to reveal the details of the hot carrier's cooling and its injection from the Au metal to the GaN substrate. Our NAMD is based on a newly developed algorithm called P-matrix formalism.[50,51] Unlike previous NAMD methods where multi-trajectory stochastic simulations are used to represent the ensemble of the trajectories to include the detailed balance and decoherence effect,[40–42,44–46] in our P-matrix formalism, a single run can represent a whole ensemble result while including the detailed balance and decoherence effect. In this formalism, the decoherence can be introduced naturally, and detailed balance is also satisfied. The efficiency of this new algorithm allows us to study various situations for relatively large systems and relatively long simulation times. By studying the detailed process of the hot carrier's pathway, different sizes of the system, different strength of the applied electric field, and addition of a hole-blocking layer, our simulation reveals the competitions between different relaxation channels, and finds a surprising result of fast carrier injection from Au nanocluster to GaN substrate before the carrier cooling down. After arriving at GaN band edge, some carriers return back to Au nanocluster. Such detailed picture of the hot carrier transfer can help us design more efficient systems to enhance the hot carrier injection efficiency.

In our NAMD simulation, we first perform a density functional theory (DFT) ground state

Born-Oppenhaimer molecular dynamics (BOMD) simulation. Its nuclear trajectory and the time-dependent Hamiltonian $\mathbf{H}(t)$ is then used to carry out the time evolution of the wave function following the time-dependent Schrödinger's equation: $i\partial\psi(t)/\partial t = \mathbf{H}(t)\psi(t)$. Different from other NAMD methods, the time-dependent Schrodinger's equation is reformulated following the P-matrix equation in a density matrix formalism.[50] In this way, it is possible to take into account the detailed balance and decoherence effect at the same time. The detailed balance is important in order to describe the cooling process, while the decoherence (dephasing) also influences the cooling rate. In this approach, we have ignored the back reaction from the electron movement to the nuclear movement. This approximation is also called classical path approximation (CPA) which are widely used in other NAMD methods.[40,41,45] Such CPA is appropriate for relatively large systems when hot carriers not highly localized, thus the back reaction from the electron movement to the nuclear movement is negligible, and the main interest of study is at the electron dynamics, not the nuclear dynamics.

We perform the plane-wave pseudopotential DFT calculation implemented in PWmat package[52,53] with the generalized gradient approximation (GGA) exchange correlation functional.[54] The atomic structure is relaxed prior to molecular dynamics (MD) simulations, and SG15 pseudopotentials[55] are used with 50 Ryd plane wave kinetic energy cutoff. Here, the pseudopotential of Au has been modified so that the position of d-orbitals in terms of the Fermi level are consistent to the experiment[56] (see Supplementary Information (SI)). Although DFT tends to underestimate work function and ionization energy for Au nanocluster and GaN surface, respectively, we find that their energy level difference for Au and GaN calculated by DFT is quite consistent with the experiments.[57–60] Therefore, the work function and ionization energy are not corrected here (see SI). Fig. 1a shows the system we have constructed. The non-polar surfaces $[11\bar{2}0]$ of GaN attaching the Au nanocluster is used to avoid surface reconstruction.[61] The Au nanocluster with 30 Au atoms is obtained via a simulated annealing using *ab initio* MD where the temperature is initially increased up to 1100 K and then cooled down slowly. A relaxation of the whole system is then performed

to reduce forces on all the atoms to be below 0.02 eV/Å. The calculated density of states is shown in Fig. 1b, where the Fermi level of Au is within the band gap of GaN. Our previous work has demonstrated that the hot carrier can be obtained in *d*-states within 50 fs upon the excitation of the plasmon in Ag_{55} nanocluster.[5] In this work, we set up initial hot holes at various *d*-states of Au nanocluster and perform NAMD to investigate their dynamics.

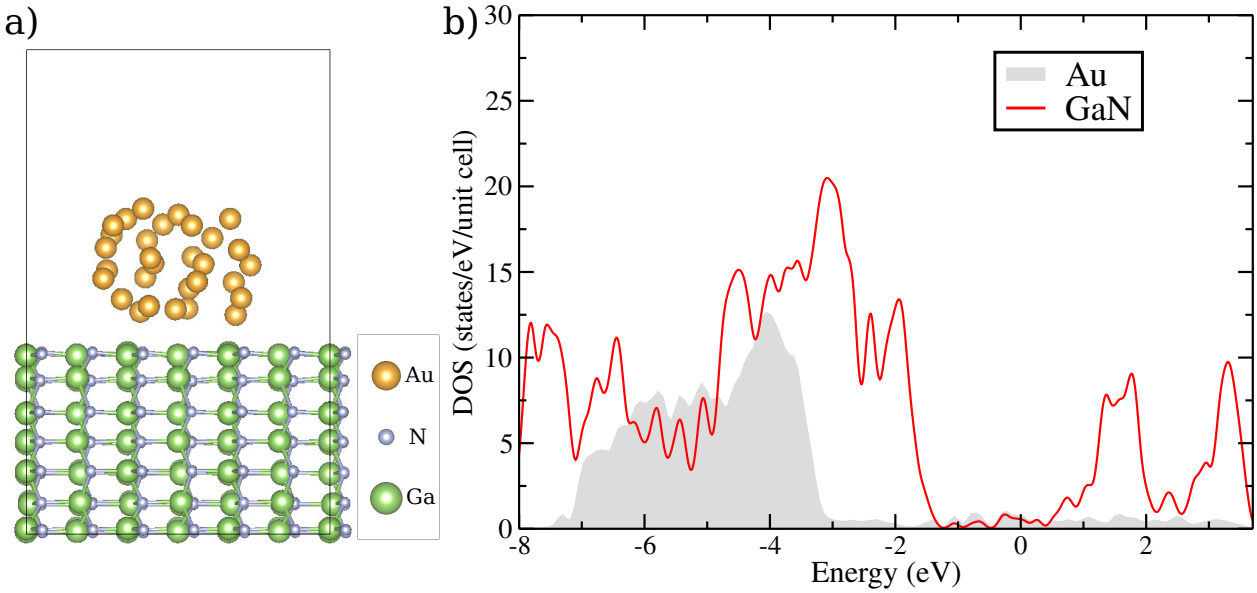

Figure 1: a) Structure of Au/GaN system under simulation (relaxed at 0K). It has 30 Au atoms and 252 GaN atoms. b) Density of states of the 0K structure projected to GaN and Au, respectively. Fermi energy is set at energy 0 eV.

In our NAMD simulation, the system is firstly simulated with a Born-Oppenheimer electronic ground state molecular dynamics (BOMD) at room temperature (300K). Then the evaluation of the carrier wavefunction is done as a post-process. The hot-carrier wavefunction $\psi_l(t)$ is evolved following the Schrödinger's equation, and it is expanded with the adiabatic basis $\phi_i(t)$ as $\psi_l(t) = \sum_i C_i^l \phi_i(t)$. Using the density matrix formalism, the density matrix of the system is $D_{ij}(t) = \sum_l w_l C_i^{l*}(t) C_j^l(t)$, under the basis of $\phi_i(t)$, where w_l is the weight of ψ_l. Due to this w_l, a $D_{ij}(t)$ can represent an ensemble of wavefunction trajectories. Following the time-dependent Schrödinger's equation, the equation of motion for the density matrix can be written down as:[50]

$$\frac{\partial}{\partial t} D_{ij}(t) = -i \left[V(t), D(t) \right]_{ij} - (1 - \delta_{ij}) \frac{D_{ij}(t)}{\tau_{ij}(t)} \tag{1}$$

and $V_{ij}(t) = \delta_{ij}\epsilon_i(t) - i \langle \phi_i(t) | \partial \phi_j(t)/\partial t \rangle$ contains the information of the change of adiabatic state $\phi_i(t)$, which implicitly includes the effect of the electron-phonon coupling. The second term is used to introduce the decoherence where $\tau_{ij}(t)$ represents the decoherence time between state i and j. To introduce the detailed balance, a P-matrix formalism is used where the density matrix $\mathbf{D}$ is splitted into $\mathbf{D} = \mathbf{P} + \mathbf{P}^{\mathrm{T}}$ with P_{ij} describing electronic state population transition from state i to j (note $P_{ij} \neq P^*_{ji}$). More explicitly, the diagonal elements of the density matrix ($D_{ii} = 2P_{ii}$) evolves as:[50]

$$\begin{aligned} \frac{\partial}{\partial t} P_{ii} = & - \mathrm{Re} \left(i \left[V, P \right]_{ii} \right) \\ & + \sum_j \mathrm{Re} \left(i P_{ij} V_{ji} \right) f_{ij} \left(e^{-|\Delta \epsilon_{ij}|\beta} - 1 \right) \\ & - \sum_j \mathrm{Re} \left(i P_{ji} V_{ij} \right) (1 - f_{ij}) \left(e^{-|\Delta \epsilon_{ij}|\beta} - 1 \right), \end{aligned} \tag{2}$$

while the off-diagonal element of P evolves as:

$$\frac{\partial}{\partial t} P_{ij} = -i \left[V, P \right]_{ij} - i V_{ij} \left(P_{ii} + P^*_{jj} \right) - \frac{P_{ij}}{\tau_{ij}} \tag{3}$$

$\Delta \epsilon_{ij} = \epsilon_i - \epsilon_j$, and f_{ij} =1 (0) for $\Delta \epsilon_{ij} > 0$ and f_{ij} =0 (1) for $\Delta \epsilon_{ij} < 0$ for an electron (hole) dynamics. The last two terms in equation 2 introduce the detailed balance, while the last term in equation 3 introduces the decoherence. For details of the derivation, we refer to our previous publications.[50,51] Combining with CPA, a ground state BOMD simulation is first executed. During such simulation, it yields the adiabatic eigen state and eigen energy pairs at MD step

T_n as $\{\phi_i(T_n), \epsilon_i(T_n)\}$. The overlapping matrix $S_{ij}(T_n, T_{n+1}) = \langle\phi_i(T_n)|\phi_j(T_{n+1})\rangle$ is recorded. Here the time step dT of BOMD simulation ($dT = T_{n+1} - T_n$) is around 1 or 2 fs. With the overlapping matrix, using the eigen state $\{\phi_i(T_n)\}$ as the basis set, the Kohn-Sham Hamiltonian at time T_n is: $H_{ij}(T_n) = \epsilon_i(T_n)\delta_{ij}$, while the Hamiltonian at next MD time step T_{n+1} with the *same* basis $\{\phi_i(T_n)\}$ becomes: $H_{ij}(T_{n+1}) = \sum_k S_{ij}(T_n, T_{n+1})\epsilon_k(T_{n+1})S_{ij}{}^*(T_n, T_{n+1})$. Here we assume $S_{ij}(T_n, T_{n+1})$ is a unitary matrix. In practice, a Gram-Schmidth approximation is used to enforce its unitarity. Knowing $H_{ij}(T_n)$ and $H_{ij}(T_{n+1})$ allows us to linearly interpolate the Hamiltonian $H_{ij}(t)$ at any time t within the interval $[T_n, T_{n+1}]$. This effectively reduces the original plane wave Hamiltonian to a small $N \times N$ Hamiltonian, where N is the number of $\phi_i(T_n)$ kept in the basis set.[51] To evolve the carrier dynamics following equation 2 and 3, a small time step dt is used from T_n to T_{n+1}. Thus, $H_{ij}(t)$ matrix is diagonalized at every dt step between T_n and T_{n+1} to get its adiabatic states $\phi_i(t)$ under the basis of $\phi_i(T_n)$, and $\phi_i(t)$ is used to evaluate $V_{ij}(t)$. In our system, N is more than 300. In practice, it is still a challenge to integrate $\mathbf{P}(t)$ from T_n to T_{n+1} at every dt step following equation 2 and 3. This is because a small dt is needed due to the possible sharp peaks in evaluating $V_{ij}(t)$ caused by the derivative $\partial\phi_j(t)/\partial t$. This happens when two $\phi_j(t)$ states cross each other, thus their identities exchanged. Such small dt can result in several thousand steps between T_n and T_{n+1}. Since each t step requires a $N \times N$ matrix diagonalization of $H_{ij}(t)$ to get $\phi_i(t)$ to evaluate $V_{ij}(t)$, this can be quite expensive. For a complex system with several hundreds adiabatic states like the interfacial system we are studying, the NAMD simulation can take days even to accomplish a few MD steps.

To solve this problem, in the current study, we have modified the implementation of NAMD. Instead of diagonalizing the Hamiltonian every dt step from T_n to T_{n+1}, we split $dT = T_{n+1} - T_n$ into M time-intervals with equal length $\delta t = dT/M$ (M is around 100 and δt is in the order of 0.01 fs). The start of each time-interval is labeled as t_m (thus $t_m = T_n + m\delta t$) with $m = 0, 1, ..., M$. In the modified NAMD, during one δt time-interval from t_m to t_{m+1}, instead of using $V_{ij}(t)$, the $\mathbf{P}$ matrix will be evolved using a fixed basis set $\phi_i(t_m)$ which

is the adiabatic eigen state obtained at time t_m.The corresponding equation is equation 4. From t_m to t_{m+1}, there is no need for matrix diagonalization, and $\mathbf{H}(t)$ is obtained from interpolation under the basis $\phi_i(t_m)$. The diagonalization of the Hamiltonian is only needed at the start of each time-interval (t_m) to obtain the basis $\phi_i(t_m)$. In this way, the number of diagonalization operations can be reduced from several thousands to only 100 within one MD step dT. More specifically, we have:

$$\frac{\partial}{\partial t}P_{ij,m}(t) = -i\left[H_m(t), P_m(t)\right]_{ij}. \tag{4}$$

for $t \in [t_m, t_{m+1}]$. Here, $\mathbf{H}_m(t)$, $\mathbf{P}_m(t)$ mean the matrix under the basis of $\phi_i(t_m)$. Thus, if we have solved $\phi_i(t_m) = \sum_j S_{ij}(T_n, t_m)\phi_j(T_n)$ ($\mathbf{S}_m(T_n, t_m)$ is the eigen-vector of the diagonalization performed at time t_m), $\mathbf{H}_m(t) = \mathbf{S}(T_n, t_m)\mathbf{H}_{T_n}(t)\mathbf{S}^\star(T_n, t_m)$, and $\mathbf{H}_{T_n}(t)$ is the interpolated Hamiltonian under $\phi_i(T_n)$ basis. To evolve equation 4 from t_m to t_{m+1}, not only one does not to diagonalize the Hamiltonian, there is also no sharp peaks to $\mathbf{H}_m(t)$. It makes the time evolution relatively easy. At time t_{m+1}, one diagonalizes the $\mathbf{H}_{T_n}(t_{m+1})$ to obtain $\phi_i(t_{m+1})$, then converts $\mathbf{P}_m(t_{m+1})$ to $\mathbf{P'}_{m+1}(t_{m+1}) = \mathbf{S}(t_m, t_{m+1})\mathbf{P}_m(t_{m+1})\mathbf{S}^\star(t_m, t_{m+1})$. Here, $S_{ij}(t_m, t_{m+1}) = \langle\phi_i(t_m)|\phi_j(t_{m+1})\rangle$. After this step, the decoherence and detailed balance can be added as:

$$\begin{aligned} P_{ii,m+1}(t_{m+1}) = P'_{ii,m+1}(t_{m+1}) &+ \sum_j \mathrm{Re}\left[\langle\phi_j(t_m)|\phi_i(t_{m+1})\rangle\, P'_{ij,m+1}(t_{m+1})\right] f_{ij}\left(e^{-|\Delta\epsilon_{ij}|\beta} - 1\right) \\ &- \sum_j \mathrm{Re}\left[\langle\phi_i(t_m)|\phi_j(t_{m+1})\rangle\, P'_{ji,m+1}(t_{m+1})\right](1 - f_{ij})\left(e^{-|\Delta\epsilon_{ij}|\beta} - 1\right) \end{aligned} \tag{5}$$

for diagonal element of P_{ii}, and

$$P_{ij,m+1}(t_{m+1}) = P'_{ij,m+1}(t_{m+1}) \tag{6}$$
$$- \langle \phi_i(t_m) | \phi_j(t_{m+1}) \rangle \, P'_{ii,m+1}(t_{m+1}) + \langle \phi_i(t_{m+1}) | \phi_j(t_m) \rangle \, P'_{jj,m+1}{}^*(t_{m+1})$$
$$- P'_{ij,m+1}(t_{m+1}) \frac{t_{m+1} - t_m}{\tau_{ij}}$$

for off-diagonal elements P_{ij} $(i \neq j)$. Such $\mathbf{P}_{m+1}(t_{m+1})$ will be the starting point for the next $[t_{m+1}, t_{m+2}]$ interval calculation using equation 4. Note, in equation 5 and 6, the $\langle \phi_i(t_m) | \phi_j(t_{m+1}) \rangle$ term is used to approximate $V_{ij} \cdot (t_{m+1} - t_m)$ term in equation 2 and 3. To evaluate equation 4 from t_m to t_{m+1}, high order expansion of $e^{i\mathbf{H}dt}$ can be used. However, we find higher orders give negligible improvement over the first-order formalism. The equation 4-6 are approximations of equation 2 and 3. In reality, our test shows that the results using equation 4-6 are almost indistinguishable from the results by equation 2 and 3, although the new equations can be hundreds of times faster if large basis set N is used. From the density matrix $\mathbf{D}$, the charge density of system at time t can be computed as $\rho(\mathbf{r}, t) = \sum_{ij} D_{ij}(t) \phi_i^*(\mathbf{r}, t) \phi_j(\mathbf{r}, t)$. All the NAMD simulations shown below are tested to converge over dt used in equation 4 (dt is set to be 0.0005 fs) and the number of diagonalizations (value of M) between two MD steps is 100. Although *ab initio* MD takes days, the post-processing NAMD only requires a few hours.

We choose one of the adiabatic eigen states characterized by Au d-states as the initial position of the hot hole. For all the NAMD simulations, the initial state is chosen so that more than 85% charges are on Au (see SI Fig.1 for one example). Fig. 2a shows evolution of the energy and the occupation density (defined as $D_{\mathrm{occ}}(E, t) = \sum_i D_{ii}(t) \delta(E - \epsilon_i(t))$ changing with time starting from the initial state. Combining the Fig. 2a with the density of states in Fig. 1b, the whole process can be splitted into three periods: period 1 (from initial hole to around -3.2 eV) possesses the highest hole cooling rate. This is due to the high density of states from both GaN p- and Au d-states. The density of states reduces during period

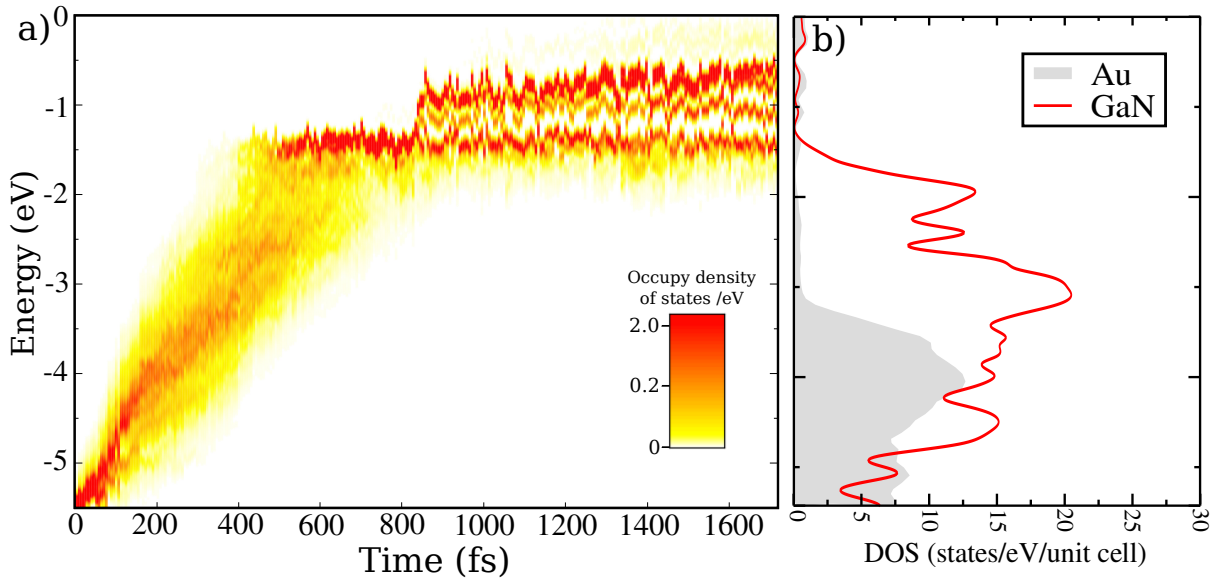

Figure 2: a) Eigen energy of the adiabatic states and their occupation. The color indicates the occupy density of states ($D_{\rm occ}(E,t) = \sum_i D_{ii}(t)\delta(E-\epsilon_i(t))$ for the excited hole. b) Density of states of the structure at time=0 (same to Fig. 1b). The Fermi energy is set at energy zero.

2 (from -3.2 eV to -1.5 eV) because of the low density of states of Au contributed by only its *s*-orbital in this energy range. However, once the hole cools to the edge of GaN valence bands around 500 fs, the sudden reduction of density of states with only Au *s*-states slows down the carrier cooling significantly in period 3 (from -1.5 eV to Fermi energy at 0 eV). Particularly, the relatively sparcity of the Au eigen states within the GaN band gap may prevent the carrier from cooling to the Fermi energy within our simulation time due to the phonon bottleneck effect. Since a single-phonon energy is not high enough to satisfy the energy conservation between different electronic states, the carrier has to wait for a long time for a multi-phonon scattering process to jump to lower energy states. We have tested the simulation up to 4 ps, the occupation of the carrier near the Fermi level is still not significant at the end of the simulation. In the above simulation, the initial energy of the hot hole relative to Fermi energy is relatively low compared to the typical laser energy used to excite the plasmon. However, we have also calculated several cases with different initial

energies of the hole (all starting from Au *d*-state), they all show similar cooling rate and pathways (SI Fig. 3).

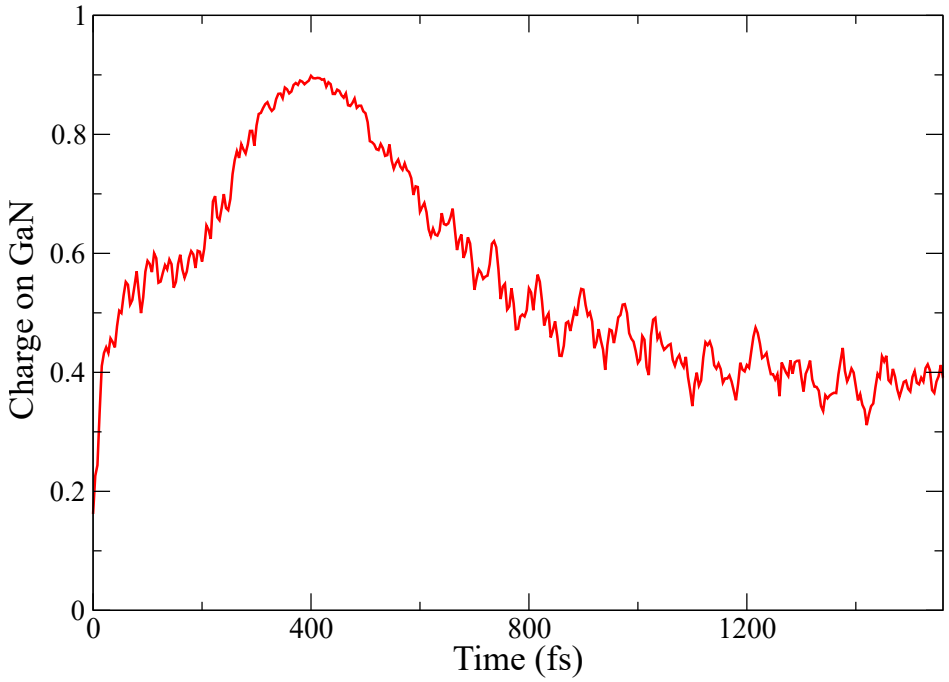

Figure 3: Charge on GaN along with time. The red line is averaged over 20 trajectories. When the charge is counted, charges below the middle line of bottom layer of Au and top layer of GaN are counted as the charge of GaN; otherwise as the charge of Au.

In addition to the above energy analysis for the hole's motion, it is possible to analyze its spatial transfer pathways across the interface. In a way, this is already partially shown in Fig. 2, since the density of states (Fig. 2b) illustrates the dominant character of the eigen states within an energy range as GaN, Au or their mix. Fig. 3 shows the charge distributed on GaN as a function of time in a more direct way. Here, we have simulated 20 different initial configurations. The curve is the averaged charge distribution over these 20 simulations. Note, each P-matrix simulation already includes an ensemble of trajectories starting with the same initial wave function and with the same nuclear trajectory. At the starting point, the majority of the hole-charges are on Au as aforementioned. However, these charges quickly expand to GaN to 50% GaN-occupation within 50 fs. Such fast process is also consistent to previous theoretical investigations.[41,42] From 50 fs to around 200 fs, the

occupation of charge on GaN is a rough plateau around 55%. Together with Fig. 2, we find that this period corresponds to the carrier cooling within the Au *d*-state until it reaches the bottom of *d*-state (period 1). The 55% occupation may be due to similar density of states between GaN and Au in this energy region (Fig. 2b). Using a larger Au nanocluster will shorten this period. This can be observed in the simulation of a 60-Au nanocluster shown in SI Fig. 5, where the net increase of the density of states caused by larger Au cluster reduces the "plateau" time but also decreases the distribution of charge in GaN during this plateau. After 200 fs in Fig. 3, the hot hole begins to transfer to GaN, and nearly 90% of the hole is inside GaN at around 400 fs. Referring back to Fig. 2a and 2b, one can see that starting from around 300fs, at the hot carrier's energy region, the Au only has its *s*-state density of states, and the majority of the density of states comes from GaN. At around 400 fs, the carrier reaches the top of the valence state in GaN, and the maximum occupation in GaN is also reached. After 400 fs, the occupation inside GaN begins to reduce, indicating a back-flow to Au for it to reach the Fermi energy in Au. Overall, our simulation demonstrates that the *majority* of the hot hole tends to cross the interface quickly instead of waiting inside Au until it has cooled down to the edge of *d*-state and all the way to the Fermi energy. The carrier immediately spreads out to GaN before it is cooled down to the bottom of Au-*d* states. Although Au nanocluster is only weakly binded to GaN, the vdW nature of the interaction does not prevent the hole-charge from jumping from Au to GaN. One might wonder whether this fast spread of carrier localization is due to the small size of the simulated Au cluster, which might be difficult to contain the carrier wavefunctions (SI Fig. 1a). But the similar behavior is observed when we increase the Au nanocluster size from 30 to 60 atoms. As shown in SI Fig. 5, the Au 60-atom case is much alike the Au 30-atom case. Nevertheless, we do see some differences. First, the maximum transfer charge to GaN has reduced slightly from 90% to 85%, and the charge plateau before the carrier reaches the top of Au-*d* states has also reduced from about 55% to 45%. But note that all these reduction is not inversely proportional to the Au nanocluster size, which has doubled

from 30 atoms to 60 atoms. Comparing Fig. 3 with SI Fig. 5, the biggest difference comes from the time to reach the maximum. Roughly, the cooling rate in the Au 60-atom case is twice as fast as the case in Au 30-atom case. This means that small Au 30-atom nanocluster suffers strongly from its phonon-bottleneck effect, and the electron-phonon coupling inside the Au nanocluster dominates the initial cooling process, despite the fact more than half of the carrier wavefunction is outside the Au nanocluster.

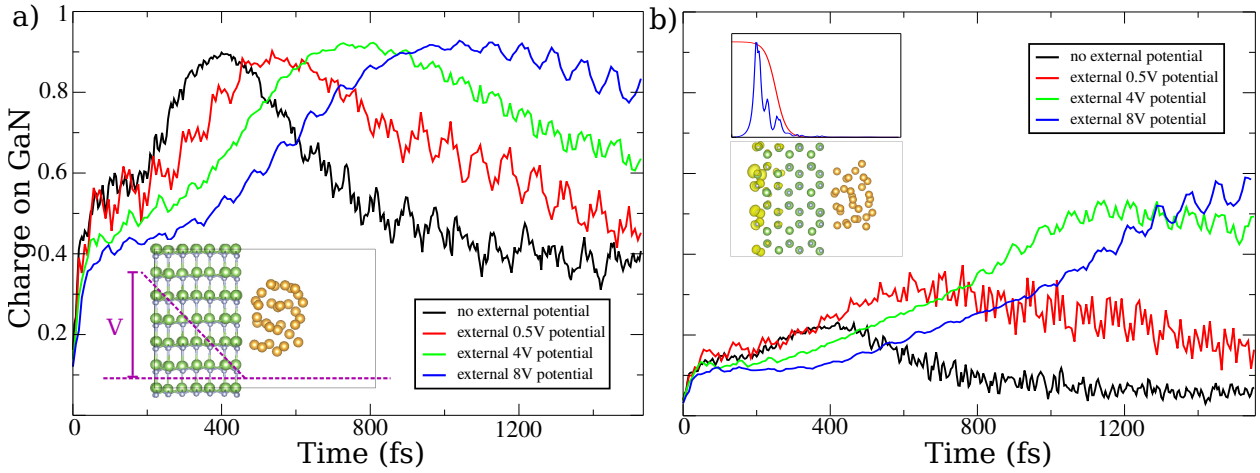

Figure 4: a) Total hole charge in GaN under different external potentials. Inset: the scheme of the applied external potential. b) Charge occupation in the mask region under different external potentials. Inset: (bottom) localized charge density of one adiabatic state under the external potential of 8V, (top) its charge density averaged in x-y plane (blue curve), and the mask function (red curve). To simplify the analysis, charges below the middle line between bottom layer of Au and top layer of GaN are treated belonging to GaN; otherwise they will be counted as charge of Au.

After the majority of the hole are transferred to GaN, we observe that some holes return back to Au after they cool down to the valence band edge of GaN. In Fig. 3, the hole distribution on GaN starts to decrease to only around 40% from 400 fs up to 1200 fs. It shows that less than half of the holes stay on GaN, but other holes return back to Au. Such back transfer has been observed in previous experimental and theoretical works.[22,40,42] Particularly, the nonlinear optical technique reveals the returning of the transferred electron is on picosecond time scale,[22] closing to the time of the hole's returning in our calculation. Thus, it is something to be prevented since it reduces the eventual carrier harvesting. It

will be quite useful to engineer the interface to reduce this back transfer. Before we discuss different ways to mitigate this back flow, it is worth to discuss first the possible artifacts which contribute to this back flow. In a real system, when the charge is transferred out of Au, it can move into the bulk of GaN far away from Au nanocluster, thus never returns. To show the back flow due to the finite size of the system, we perform a simulation of the same system but putting the initial hole in the GaN above the *d*-state of Au (see SI). We find that the "warm" hole (its energy is above the Au *d*-state) spreads from GaN to Au in very similar fashion as the back transfer case shown in Fig.3 (SI Fig.4). Our calculation demonstrates that the back flow is non-avoidable given the small GaN layer we can afford. We believe due to the limited GaN layers in our simulation, the effect of back flow is probably overestimated. Nevertheless, we should still be able to design heterostructures to enhance the hole transfer to GaN, as the qualitative trend should still be the same. The relative values of the back flow to Au should still be a good indicator.

The experiments of the heterostructure Au/p-type GaN illustrated in Ref. 16 and 23 demonstrate the hole harvesting from Au to GaN. The Schottky-barrier band bending in this system has been shown to play a central role to assist the hole transfer. The careful design of such heterostructure allows the formation of the internal electric field near the interface resulting from the band bending in the depletion layers. Such electric field can drive the hole away and reduce their back transfer. In order to demonstrate the role of the internal electric field, we perform MD and NAMD simulations under different external electric fields. Shown in Fig. 4a inset is the scheme of the external potentials added to mimic the Schottky barrier band bending. External potentials with values of 0.5V, 4V and 8V at the vacuum side end of GaN are applied linearly inside GaN, respectively. For all these cases, the states near the Fermi energy are still Au states. Thus, thermadynamically, the hole should still return to Au. Fig. 4a shows the spatial charge occupation on GaN as a function of time under different external potentials. It is interesting to see that by applying higher electric field, more holes tend to stay on GaN for a longer time, less likely to return to

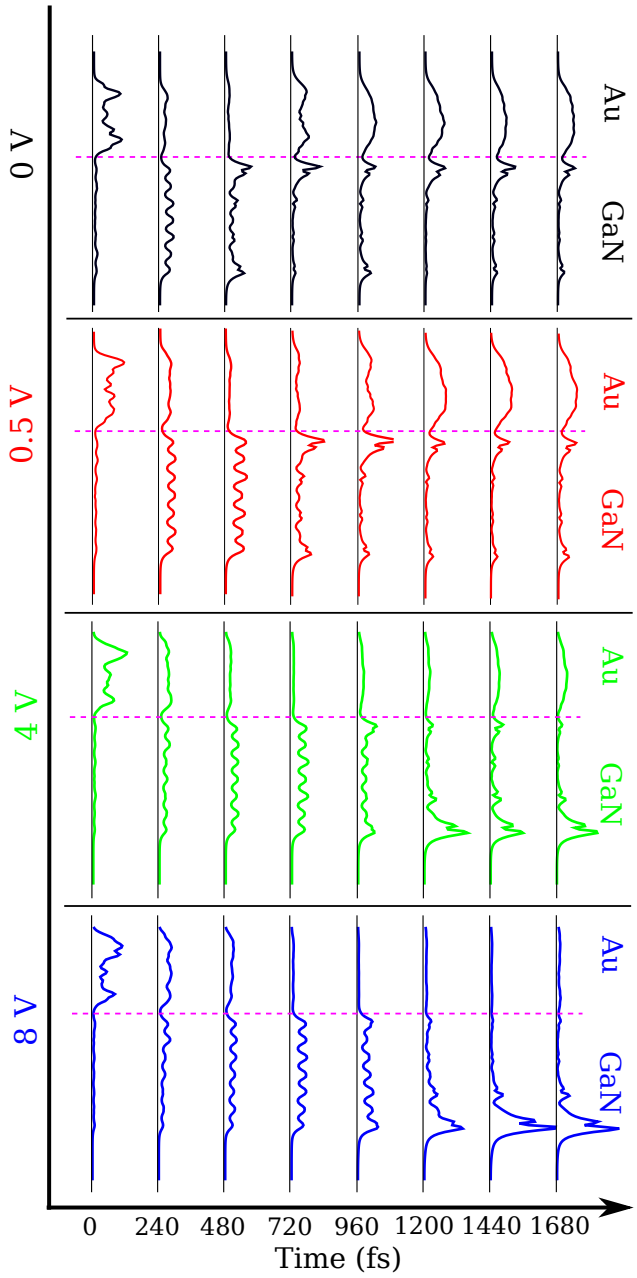

Figure 5: Charge density evolution with time under different external potentials (from top to bottom, 0V, 0.5V, 4V and 8V). Dashed magenta line separate Au and GaN regions. The charge density is averaged in $x-y$ plane of the simulation cell as $\rho(z;t) = \int \rho(x,y,z;t)dxdy$.

Au. Even a relatively low external potential of 0.5V can affect the behaviour of the excited hole noticeably. It is also interesting to see that the time of the charges arriving at GaN also becomes slower when the field strength increases. This is due to a shift of GaN density of state. The lack of density of states at higher electric field reduces the initial charge transfer rate. In order to further understand the charge distribution inside GaN. Fig. 4b illustrates the charge distribution of the localized adiabatic state within a "mask" region at the end of GaN in its vacuum side as shown in the inset. We use a mask function to capture such state. This mask $m(\mathbf{r})$ is then used to calculate $\int \rho(\mathbf{r},t)m(\mathbf{r})d^3\mathbf{r}$, and the result is shown in Fig. 4b. As we have discussed above, our calculation may overestimate the amount of the charge returning to Au and have almost 100% return of the charge to Au if the running of our calculation is infinitely long, since the states at Fermi energy is localized inside Au. It is thus helpful if we can define a measure of charge density inside GaN, and assume the measured charge to disappear into the bulk of GaN in an infinite GaN system. One such measure is the trapped charge within that mask. It is reasonable to assume that once the charge is "trapped" in this mask region, it can be considered as going to the bulk GaN, and never returns. Thus, we can use the highest amplitude of the charge inside the mask region during the simulation time to provide a quantitative measure of the total charge captured by the bulk GaN. The subsequent decay of the charge within the mask region is due to the back flow to higher energy Au state owing to the finite size of the simulated system. Note, this is probably a lower-limit estimation, since before it reaches the maximum, some of the charge might already return to the Au due to the finite GaN size (hence once again, overestimation of the back flow). Besides, the mask function itself only calculates the state near the end of GaN, thus can miss other states of GaN. Nevertheless, we can use these numbers to provide an estimate. Under the external potentials of 0, 0.5, 4, and 8V, we get the maximum charge of 22%, 35%, 50% and 60%, respectively.

To further understand the details of the charge distribution in real space, Fig. 5 illustrates the charge density chosen from one initial state run averaged over x-y plane under different

external potentials (from top to bottom: 0V, 0.5V, 4V and 8V) as a function of time. All the cases show a sub-picosecond fast charge transfer from Au to GaN. For 0 V, the charges on GaN never stay significantly in the mask region. For 0.5 V case, there is a slight distribution in this region, but most of the charge escapes to Au eventually. When the electric field increases further, the mask regions start to be populated clearly after the charges are transferred to GaN, indicating the efficiency of the band bending to assist the hole transfer in Au/GaN heterostructure.

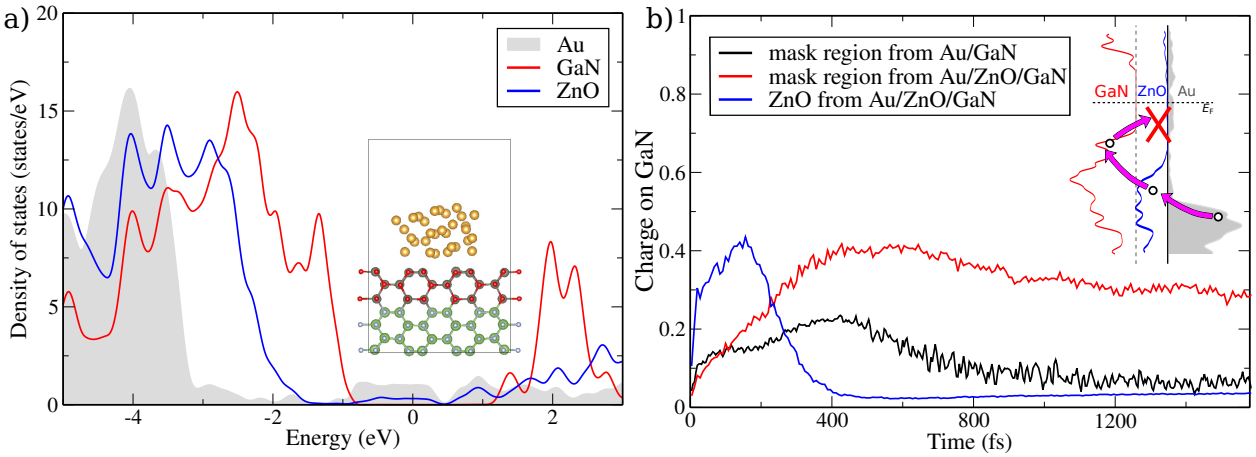

Figure 6: a) The projected density of states of Au, ZnO and GaN. Inset: relaxed structure of Au/ZnO/GaN heterostructure at 0K (Red: oxygen atom, Dark grey: zinc atom). b) The charge distribution of GaN and ZnO compared to the pure Au/GaN system. The mask region is the same to the pure Au/GaN case (Fig. 4b). Inset: illustration of the role of ZnO in preventing the hole from returning back to Au after it reaches the band edge of GaN. But the initial hot hole transfer from Au to GaN is not affected by ZnO.

In addition to the Schottky barrier and its induced internal electric field, following our understanding of the charge back flow, we propose to use a hole-block layer to prevent the back flow. Such inserted layer separates GaN and Au wavefunction spatially to reduce their coupling, hence to prevent the back flow of the equilibrized hole carrier. On the other hand, the inserted layer should have a potential barrier low enough so that it will not block the initial hot carrier transfer from Au to GaN. We find ZnO is a good choice. Similar to GaN, ZnO possesses wide band gap. Its valence band maximum is around 0.8 eV lower than that of GaN, roughly at the same level of *d*-states edge of Au.[58] Interestingly, ZnO

has quite similar structure (Wurtzite crystal shape) and lattice constants to GaN, which brings a great advantage for high quality synthesis as well as theoretical simulation. In our calculation, we replace top three layers of GaN by ZnO (Fig. 6a inset), relax the whole structure, and compute the projection of the density of states. Fig. 6a shows the position of the ZnO states, which is consistent to the experiments.[57,58,62,63] By performing MD and post-processing NAMD simulations, the time-dependent spatial charge distribution on GaN is obtained, and shown in Fig. 6b. Similar to the case of Au/GaN, the hot hole transfers to GaN by passing through ZnO. This initial charge transfer is not significantly reduced by the existence of ZnO. After the charge reaches the band edge of GaN and becomes an equilibrium "cold" carrier, the potential created by ZnO effectively reduces the coupling between GaN and Au, and diminishes the back flow to Au. Using the same approach as for the external potential case, we obtain the maximum amount of charge transfer in the mask region. We get a value of more than 40%, which is much higher than the 22% of the pure Au/GaN structure. The effect of the three layer of ZnO is equivalent to an applied external potential between 0.5 and 4V. Furthermore, when the amount of charges inside the mask region reaches the maximum, its subsequent reduction also becomes slower compared to pure Au/GaN case even with an external potential. It further shows the effectiveness of ZnO layer lowering the back flow from GaN to Au.

In summary, we have performed a detailed hot hole dynamics with quantum mechanics non-adiabatic molecular dynamics simulation for the heterostructure Au/GaN. By setting up the hole initially at Au *d*-state, the *ab initio* MD and the post-processing NAMD reveal that the time-scale for the hole transfer is less than 200 fs. The excited hole first cools to the band edge of Au *d*-state, while at the mean time spread out into GaN. The majority of the charge then quickly cool down further to the edge of GaN. We also observe that some of the charge can return back to Au after it reaches the band edge of GaN. To understand the role of band bending in Schottky barrier, different external potentials are applied. The NAMD simulation shows that the internal electric field can indeed enhance the hole transfer

from Au to GaN. Using a special technique of GaN edge trapping state, we estimate the lower limit of total charge transfer amplitude when the external potential is 0, 0.5, 4 and 8V, as 22%, 35%, 50% and 60%, respectively. We also propose a ZnO insertion layer between GaN and Au to prevent the back flow of the "cold" hole, while keep the initial hot carrier flowing from Au to GaN. We find more than 40% electron transfer to GaN when ZnO layer is used, this is to compare with the 22% electron transfer without the ZnO hole-block layer. Finally, we also find that increasing the Au nanocluster from 30-atom to 60-atom will speed up the hot carrier cooling rate significantly, but only slightly reduce the hot carrier transfer amplitude from Au to GaN. This indicates that the cooling is predominatly caused by the electron-phonon coupling within Au, and the phonon bottleneck plays an important role. Our calculation demonstrates that the newly developed P-matrix method can be used to study carrier dynamics for systems with hundreds of atoms, and to simulate the dynamics for multiple picoseconds.

Acknowledgement

This material is based on the work performed by the Joint Center for Artificial Photosynthesis, a DOE Energy Innovation Hub, supported through the Office of Science of the U.S. Department of Energy under Award number DE-SC0004993. We use the resource of National Energy Research Scientific Computing center (NERSC) located in Lawrence Berkeley National Laboratory and the computational resource of the Oak Ridge Leadership Computing Facility at the Oak Ridge National Laboratory under the Innovative and Novel Computational Impact on Theory and Experiment project.

References

(1) Mukherjee, S.; Libisch, F.; Large, N.; Neumann, O.; Brown, L. V.; Cheng, J.; Lassiter, J. B.; Carter, E. A.; Nordlander, P.; Halas, N. J. Hot Electrons Do the Impossible:

Plasmon-Induced Dissociation of H2 on Au. *Nano Letters* **2013**, *13*, 240–247.

(2) Moskovits, M. The Case for Plasmon-Derived Hot Carrier Devices. *Nature Nanotechnology* **2015**, *10*, 6–8.

(3) Clavero, C. Plasmon-Induced Hot-Electron Generation at Nanoparticle/Metal-Oxide Interfaces for Photovoltaic and Photocatalytic Devices. *Nature Photonics* **2014**, *8*, 95–103.

(4) Christopher, P.; Moskovits, M. Hot Charge Carrier Transmission from Plasmonic Nanostructures. *Annual Review of Physical Chemistry* **2017**, *68*, 379–398.

(5) Ma, J.; Wang, Z.; Wang, L.-W. Interplay between Plasmon and Single-Particle Excitations in a Metal Nanocluster. *Nature Communications* **2015**, *6*, 10107.

(6) Robatjazi, H.; Bahauddin, S. M.; Doiron, C.; Thomann, I. Direct Plasmon-Driven Photoelectrocatalysis. *Nano Letters* **2015**, *15*, 6155–6161.

(7) Zhong, Y.; Ueno, K.; Mori, Y.; Shi, X.; Oshikiri, T.; Murakoshi, K.; Inoue, H.; Misawa, H. Plasmon-Assisted Water Splitting Using Two Sides of the Same SrTiO3 Single-Crystal Substrate: Conversion of Visible Light to Chemical Energy. *Angewandte Chemie International Edition* **2014**, *53*, 10350–10354.

(8) Mubeen, S.; Lee, J.; Singh, N.; Krämer, S.; Stucky, G. D.; Moskovits, M. An Autonomous Photosynthetic Device in Which All Charge Carriers Derive from Surface Plasmons. *Nature Nanotechnology* **2013**, *8*, 247–251.

(9) Marimuthu, A.; Zhang, J.; Linic, S. Tuning Selectivity in Propylene Epoxidation by Plasmon Mediated Photo-Switching of Cu Oxidation State. *Science* **2013**, *339*, 1590–1593.

(10) Christopher, P.; Xin, H.; Linic, S. Visible-Light-Enhanced Catalytic Oxidation Reactions on Plasmonic Silver Nanostructures. *Nature Chemistry* **2011**, *3*, 467–472.

(11) Wu, B.; Liu, D.; Mubeen, S.; Chuong, T. T.; Moskovits, M.; Stucky, G. D. Anisotropic Growth of TiO2 onto Gold Nanorods for Plasmon-Enhanced Hydrogen Production from Water Reduction. *Journal of the American Chemical Society* **2016**, *138*, 1114–1117.

(12) Zhou, L.; Zhang, C.; McClain, M. J.; Manjavacas, A.; Krauter, C. M.; Tian, S.; Berg, F.; Everitt, H. O.; Carter, E. A.; Nordlander, P.; Halas, N. J. Aluminum Nanocrystals as a Plasmonic Photocatalyst for Hydrogen Dissociation. *Nano Letters* **2016**, *16*, 1478–1484.

(13) Mukherjee, S.; Zhou, L.; Goodman, A. M.; Large, N.; Ayala-Orozco, C.; Zhang, Y.; Nordlander, P.; Halas, N. J. Hot-Electron-Induced Dissociation of H2 on Gold Nanoparticles Supported on SiO2. *Journal of the American Chemical Society* **2014**, *136*, 64–67.

(14) Mubeen, S.; Lee, J.; Liu, D.; Stucky, G. D.; Moskovits, M. Panchromatic Photoproduction of H2 with Surface Plasmons. *Nano Letters* **2015**, *15*, 2132–2136.

(15) Robatjazi, H.; Zhao, H.; Swearer, D. F.; Hogan, N. J.; Zhou, L.; Alabastri, A.; McClain, M. J.; Nordlander, P.; Halas, N. J. Plasmon-Induced Selective Carbon Dioxide Conversion on Earth-Abundant Aluminum-Cuprous Oxide Antenna-Reactor Nanoparticles. *Nature Communications* **2017**, *8*, 27.

(16) DuChene, J. S.; Tagliabue, G.; Welch, A. J.; Cheng, W.-H.; Atwater, H. A. Hot Hole Collection and Photoelectrochemical CO2 Reduction with Plasmonic Au/p-GaN Photocathodes. *Nano Letters* **2018**, *18*, 2545–2550.

(17) Clark, M. L.; Ge, A.; Videla, P. E.; Rudshteyn, B.; Miller, C. J.; Song, J.; Batista, V. S.; Lian, T.; Kubiak, C. P. CO2 Reduction Catalysts on Gold Electrode Surfaces Influenced by Large Electric Fields. *Journal of the American Chemical Society* **2018**, *140*, 17643–17655.

(18) Li, J.; Cushing, S. K.; Zheng, P.; Senty, T.; Meng, F.; Bristow, A. D.; Manivannan, A.; Wu, N. Solar Hydrogen Generation by a CdS-Au-TiO2 Sandwich Nanorod Array En-

453 hanced with Au Nanoparticle as Electron Relay and Plasmonic Photosensitizer. *Journal*
454 *of the American Chemical Society* **2014**, *136*, 8438–8449.

455 (19) Furube, A.; Du, L.; Hara, K.; Katoh, R.; Tachiya, M. Ultrafast Plasmon-Induced Elec-
456 tron Transfer from Gold Nanodots into TiO2 Nanoparticles. *Journal of the American*
457 *Chemical Society* **2007**, *129*, 14852–14853.

458 (20) Tian, Y.; Tatsuma, T. Mechanisms and Applications of Plasmon-Induced Charge Sepa-
459 ration at TiO2 Films Loaded with Gold Nanoparticles. *Journal of the American Chem-*
460 *ical Society* **2005**, *127*, 7632–7637.

461 (21) Mubeen, S.; Hernandez-Sosa, G.; Moses, D.; Lee, J.; Moskovits, M. Plasmonic Pho-
462 tosensitization of a Wide Band Gap Semiconductor: Converting Plasmons to Charge
463 Carriers. *Nano Letters* **2011**, *11*, 5548–5552.

464 (22) Tisdale, W. A.; Williams, K. J.; Timp, B. A.; Norris, D. J.; Aydil, E. S.; Zhu, X.-Y. Hot-
465 Electron Transfer from Semiconductor Nanocrystals. *Science* **2010**, *328*, 1543–1547.

466 (23) Tagliabue, G.; DuChene, J. S.; Abdellah, M.; Habib, A.; Hattori, Y.; Zheng, K.; Can-
467 ton, S. E.; Gosztola, D. J.; Cheng, W.-H.; Sá, J.; Atwater, H. A. Ultrafast Studies of
468 Hot-Hole Dynamics in Au/p-GaN Heterostructures. 12.

469 (24) Du, L.; Furube, A.; Hara, K.; Katoh, R.; Tachiya, M. Ultrafast Plasmon Induced
470 Electron Injection Mechanism in Gold–TiO2 Nanoparticle System. *Journal of Photo-*
471 *chemistry and Photobiology C: Photochemistry Reviews* **2013**, *15*, 21–30.

472 (25) Wen, X.; Xu, W.; Zhao, W.; Khurgin, J. B.; Xiong, Q. Plasmonic Hot Carriers-
473 Controlled Second Harmonic Generation in WSe2 Bilayers. *Nano Letters* **2018**, *18*,
474 1686–1692.

475 (26) Yu, Y.; Ji, Z.; Zu, S.; Du, B.; Kang, Y.; Li, Z.; Zhou, Z.; Shi, K.; Fang, Z. Ultrafast

Plasmonic Hot Electron Transfer in Au Nanoantenna/MoS2 Heterostructures. *Advanced Functional Materials* **2016**, *26*, 6394–6401.

(27) Anderson, N. A.; Lian, T. ULTRAFAST ELECTRON TRANSFER AT THE MOLECULE-SEMICONDUCTOR NANOPARTICLE INTERFACE. *Annual Review of Physical Chemistry* **2005**, *56*, 491–519.

(28) Grimaldi, G.; Crisp, R. W.; ten Brinck, S.; Zapata, F.; van Ouwendorp, M.; Renaud, N.; Kirkwood, N.; Evers, W. H.; Kinge, S.; Infante, I.; Siebbeles, L. D. A.; Houtepen, A. J. Hot-Electron Transfer in Quantum-Dot Heterojunction Films. *Nature Communications* **2018**, *9*, 2310.

(29) Sundararaman, R.; Narang, P.; Jermyn, A. S.; Goddard Iii, W. A.; Atwater, H. A. Theoretical Predictions for Hot-Carrier Generation from Surface Plasmon Decay. *Nature Communications* **2014**, *5*, 5788.

(30) Brown, A. M.; Sundararaman, R.; Narang, P.; Goddard, W. A.; Atwater, H. A. Nonradiative Plasmon Decay and Hot Carrier Dynamics: Effects of Phonons, Surfaces, and Geometry. *ACS Nano* **2016**, *10*, 957–966.

(31) Govorov, A. O.; Zhang, H.; Gun'ko, Y. K. Theory of Photoinjection of Hot Plasmonic Carriers from Metal Nanostructures into Semiconductors and Surface Molecules. *The Journal of Physical Chemistry C* **2013**, *117*, 16616–16631.

(32) Zhou, J.-J.; Hellman, O.; Bernardi, M. Electron-Phonon Scattering in the Presence of Soft Modes and Electron Mobility in $SrTiO_3$ Perovskite from First Principles. *Physical Review Letters* **2018**, *121*, 226603.

(33) Bernardi, M.; Vigil-Fowler, D.; Lischner, J.; Neaton, J. B.; Louie, S. G. Ab Initio Study of Hot Carriers in the First Picosecond after Sunlight Absorption in Silicon. *Physical Review Letters* **2014**, *112*, 257402.

(34) Marcus, R. A. On the Theory of Oxidation-Reduction Reactions Involving Electron Transfer. I. *The Journal of Chemical Physics* **1956**, *24*, 966–978.

(35) Wei, H.; Luo, J.-W.; Li, S.-S.; Wang, L.-W. Revealing the Origin of Fast Electron Transfer in TiO2-Based Dye-Sensitized Solar Cells. *Journal of the American Chemical Society* **2016**, *138*, 8165–8174.

(36) Liu, Y.-Y.; Zheng, F.; Jiang, X.; Luo, J.-W.; Li, S.-S.; Wang, L.-W. *Ab Initio* Investigation of Charge Trapping Across the Crystalline- Si –Amorphous- Si O 2 Interface. *Physical Review Applied* **2019**, *11*, 044058.

(37) Tarafder, K.; Surendranath, Y.; Olshansky, J. H.; Alivisatos, A. P.; Wang, L.-W. Hole Transfer Dynamics from a CdSe/CdS Quantum Rod to a Tethered Ferrocene Derivative. *Journal of the American Chemical Society* **2014**, *136*, 5121–5131.

(38) Chu, I.-H.; Radulaski, M.; Vukmirovic, N.; Cheng, H.-P.; Wang, L.-W. Charge Transport in a Quantum Dot Supercrystal. *The Journal of Physical Chemistry C* **2011**, *115*, 21409–21415.

(39) Duncan, W. R.; Craig, C. F.; Prezhdo, O. V. Time-Domain Ab Initio Study of Charge Relaxation and Recombination in Dye-Sensitized TiO2. *Journal of the American Chemical Society* **2007**, *129*, 8528–8543.

(40) Prezhdo, O. V.; Duncan, W. R.; Prezhdo, V. V. Photoinduced Electron Dynamics at the Chromophore–Semiconductor Interface: A Time-Domain Ab Initio Perspective. *Progress in Surface Science* **2009**, *84*, 30–68.

(41) Zhang, J.; Guan, M.; Lischner, J.; Meng, S.; Prezhdo, O. V. Coexistence of Different Charge-Transfer Mechanisms in the Hot-Carrier Dynamics of Hybrid Plasmonic Nanomaterials. *Nano Letters* **2019**,

(42) Long, R.; Prezhdo, O. V. Instantaneous Generation of Charge-Separated State on TiO2 Surface Sensitized with Plasmonic Nanoparticles. *Journal of the American Chemical Society* **2014**, *136*, 4343–4354.

(43) Zhang, Z.; Liu, L.; Fang, W.-H.; Long, R.; Tokina, M. V.; Prezhdo, O. V. Plasmon-Mediated Electron Injection from Au Nanorods into MoS2: Traditional versus Photoexcitation Mechanism. *Chem* **2018**, *4*, 1112–1127.

(44) Long, R.; Prezhdo, O. V. Ab Initio Nonadiabatic Molecular Dynamics of the Ultrafast Electron Injection from a PbSe Quantum Dot into the TiO2 Surface. *Journal of the American Chemical Society* **2011**, *133*, 19240–19249.

(45) Zhang, J.; Hong, H.; Zhang, J.; Fu, H.; You, P.; Lischner, J.; Liu, K.; Kaxiras, E.; Meng, S. New Pathway for Hot Electron Relaxation in Two-Dimensional Heterostructures. *Nano Letters* **2018**, *18*, 6057–6063.

(46) Long, R.; English, N. J.; Prezhdo, O. V. Photo-Induced Charge Separation across the Graphene–TiO2 Interface Is Faster than Energy Losses: A Time-Domain Ab Initio Analysis. *Journal of the American Chemical Society* **2012**, *134*, 14238–14248.

(47) Zhou, X.; Tokina, M. V.; Tomko, J. A.; Braun, J. L.; Hopkins, P. E.; Prezhdo, O. V. Thin Ti Adhesion Layer Breaks Bottleneck to Hot Hole Relaxation in Au Films. *The Journal of Chemical Physics* **2019**, *150*, 184701.

(48) Nam, Y.; Li, L.; Lee, J. Y.; Prezhdo, O. V. Strong Influence of Oxygen Vacancy Location on Charge Carrier Losses in Reduced TiO_2 Nanoparticles. *The Journal of Physical Chemistry Letters* **2019**, *10*, 2676–2683.

(49) Senanayake, R. D.; Guidez, E. B.; Neukirch, A. J.; Prezhdo, O. V.; Aikens, C. M. Theoretical Investigation of Relaxation Dynamics in $Au_{38}(SH)_{24}$ Thiolate-Protected Gold Nanoclusters. *The Journal of Physical Chemistry C* **2018**, *122*, 16380–16388.

(50) Kang, J.; Wang, L.-W. Nonadiabatic Molecular Dynamics with Decoherence and Detailed Balance under a Density Matrix Ensemble Formalism. *Physical Review B* **2019**, *99*, 224303.

(51) Ren, J.; Vukmirović, N.; Wang, L.-W. Nonadiabatic Molecular Dynamics Simulation for Carrier Transport in a Pentathiophene Butyric Acid Monolayer. *Physical Review B* **2013**, *87*, 205117.

(52) Jia, W.; Cao, Z.; Wang, L.; Fu, J.; Chi, X.; Gao, W.; Wang, L.-W. The Analysis of a Plane Wave Pseudopotential Density Functional Theory Code on a GPU Machine. *Computer Physics Communications* **2013**, *184*, 9–18.

(53) Jia, W.; Fu, J.; Cao, Z.; Wang, L.; Chi, X.; Gao, W.; Wang, L.-W. Fast Plane Wave Density Functional Theory Molecular Dynamics Calculations on Multi-GPU Machines. *Journal of Computational Physics* **2013**, *251*, 102–115.

(54) Perdew, J. P.; Burke, K.; Ernzerhof, M. Generalized Gradient Approximation Made Simple. *Physical Review Letters* **1996**, *77*, 3865–3868.

(55) Hamann, D. R. Optimized Norm-Conserving Vanderbilt Pseudopotentials. *Physical Review B* **2013**, *88*, 085117.

(56) Fadley, C.; Shirley, D. Electronic Densities of States from X-Ray Photoelectron Spectroscopy. *Journal of Research of the National Bureau of Standards Section A: Physics and Chemistry* **1970**, *74A*, 543.

(57) Hinuma, Y.; Grüneis, A.; Kresse, G.; Oba, F. Band Alignment of Semiconductors from Density-Functional Theory and Many-Body Perturbation Theory. *Physical Review B* **2014**, *90*.

(58) Stevanović, V.; Lany, S.; S. Ginley, D.; Tumas, W.; Zunger, A. Assessing Capability

of Semiconductors to Split Water Using Ionization Potentials and Electron Affinities Only. *Physical Chemistry Chemical Physics* **2014**, *16*, 3706–3714.

(59) Beach, J. D.; Collins, R. T.; Turner, J. A. Band-Edge Potentials of n-Type and p-Type GaN. *Journal of The Electrochemical Society* **2003**, *150*, A899.

(60) Singh-Miller, N. E.; Marzari, N. Surface Energies, Work Functions, and Surface Relaxations of Low-Index Metallic Surfaces from First Principles. *Physical Review B* **2009**, *80*.

(61) Lymperakis, L.; Neugebauer, J.; Himmerlich, M.; Krischok, S.; Rink, M.; Kröger, J.; Polyakov, V. M. Adsorption and Desorption of Hydrogen at Nonpolar GaN(1-100) Surfaces: Kinetics and Impact on Surface Vibrational and Electronic Properties. *Physical Review B* **2017**, *95*.

(62) Jacobi, K.; Zwicker, G.; Gutmann, A. Work Function, Electron Affinity and Band Bending of Zinc Oxide Surfaces. *Surface Science* **1984**, *141*, 109–125.

(63) Matsumoto, Y.; Yoshikawa, T.; Sato, E.-i. Dependence of the Band Bending of the Oxide Semiconductors on pH. *Journal of The Electrochemical Society* **1989**, *136*, 1389–1391.